REVISION 1

Natural Fe-bearing oxides and sulfates from the Rio Tinto Mars analogue site – Critical assessment of VNIR reflectance spectroscopy, laser Raman spectroscopy, and XRD as mineral identification tools

Pablo Sobron,[1,2,*] Janice L. Bishop,[1,3] David F. Blake,[3] Bin Chen,[3] and Fernando Rull[4]

[1]SETI Institute, 189 Bernardo Ave #100, Mountain View, California 94043, U.S.A. E-mail: psobron@seti.org

[2]MalaUva Labs, 822 Allen Ave #A, St. Louis, Missouri 63104, U.S.A.

[3]NASA Ames Research Center, Moffett Field, California 94035, U.S.A.

[4]Unidad Asociada UVA-Centro de Astrobiología. Edificio INDITI, Av.Francisco Valles 8, Parque Tecnologico de Boecillo, Parcela 203, Boecillo 47151, Spain.

ABSTRACT

We have characterized complex iron and sulfate-bearing samples from Rio Tinto (Spain) using X-ray diffraction (XRD), visible-near infrared reflectance (VNIR) spectroscopy, and laser Raman spectroscopy (LRS). Samples were collected for this study from the Peña de Hierro region of Rio Tinto because this site represents a natural acidic environment that is a potential analog for such environments on Mars. We report an evaluation of the capabilities of these three techniques in performing detailed mineralogical

characterization of potential Mars-like samples from a natural acidic terrestrial environment. Sulfate minerals found in these samples include gypsum, jarosite, and copiapite, and iron hydroxide bearing minerals found include goethite and ferrihydrite. These sulfate and iron hydroxide/oxyhydroxide minerals were detected by XRD, VNIR and LRS. Minor quartz was identified in some samples by XRD as well, but was not identified using VNIR spectroscopy. Coordinating the results from these three techniques provides a complete picture of the mineralogical composition of the samples. Field instruments were used for this study in order to mimic the kinds of analyses that could be performed in the field or on Martian rovers.

Key words: Raman, VNIR reflectance, XRD, Sulfates, Iron, Mars, Analogue, Rio Tinto

INTRODUCTION

The surface of Mars contains abundant occurrences of aqueous environments that host sulfates and iron oxide/hydroxide-bearing minerals. The detection of crystalline hematite by the Mars Global Surveyor Thermal Emission Spectrometer (MGS-TES) (Christensen et al., 2000; Christensen et al., 2001) was a main driver for the selection of Meridiani Planum as the landing site for the NASA's Mars Exploration Rover (MER) Opportunity. TES studies contributed to the understanding of the occurrence of hematite; geochemical considerations led to the conclusion that the most plausible mechanism for the occurrence of the hematite units was precipitation from Fe-rich water.

Identification of hydrous sulfates in several bright regions including Paso Robles and Tyrone at Gusev crater (Gellert et al., 2006; Haskin et al., 2005; Johnson et al., 2007; Lane et al., 2008; Ming et al., 2008; Parente et al., 2009; Wang et al., 2008; Wang et al., 2006) and the alleged findings of jarosite in the Meridiani regolith (Klingelhofer et al., 2004), at Mawrth Vallis (Farrand et al., 2009), and at Noctis Labyrinthus (Weitz et al., 2011) provide evidence for former aqueous processes on Mars.

Massive accumulations of sulfates have also been detected remotely using data from the OMEGA (Observatoire pour la Minéralogie, l'Eau, les Glaces, et l'Activité) instrument on ESA's Mars Express (Bibring et al., 2007; Gendrin et al., 2005) and the CRISM (Compact Reconnaissance Imaging Spectrometer for Mars) instrument on NASA's Mars Reconnaissance Orbiter (Bishop et al., 2009; Flahaut et al., 2010; Lichtenberg et al., 2010; Murchie et al., 2009; Roach et al., 2010; Roach et al., 2009; Sowe et al., 2012; Wiseman et al., 2010).

Sulfates were also detected at the Phoenix landing site (Smith et al., 2009). More recently, the ChemCam instrument onboard the Mars Science Laboratory rover, Curiosity, has identified the presence of Ca-sulfates at Rocknest (Clegg et al., 2013; Tokar et al., 2013). The presence of thses sulfate mineral species listed above not only constitutes evidence regarding the environmental conditions in the history of a particular region (Meslin et al., 2013), but may define the potential habitability of an environment (Boston et al., 2001).

The Rio Tinto acid mine drainage-dominated region provides numerous environments where sulfates and iron oxide/hydroxide species have formed (Amils et al., 2007; Fernandez-Remolar et al., 2005; Fernández-Remolar et al., 2011). These studies have shown that both inorganic and biologic activity plays a role in formation of many of the precipitates and efflorescent salts in this region. Given the association of microorganisms such as *Acidithiobacillus ferrooxidans* with the aqueous oxidation of sulfides in Rio Tinto (Amils et al., 2002), deposits of sulfate precipitates on Mars represent possible sites to search for extinct life on that planet.

Lab and field investigations of iron-rich aqueous precipitates and alteration environments are needed in order to provide ground-truthing for identification of these minerals on Mars and in order to improve our ability to connect the Martian mineralogy to geochemical environments. For this study, we used three techniques for a mineralogical investigation that are currently employed or planned for landed missions on Mars: X-ray diffraction (XRD), visible-near infrared (VNIR) reflectance spectroscopy, and laser Raman spectroscopy (LRS).

The goals of our investigation are to: (1) characterize the complex iron and sulfate-bearing samples from a site at Rio Tinto (SW Spain); (2) compare measurement type, analysis and results of these three techniques to perform detailed mineralogical characterization of potential Mars-like samples from a natural acidic terrestrial environment; and (3) provide a collection of diffraction and spectral data that can help interpret mission data.

METHODS

Samples

Efflorescences and precipitates associated with acidic surface stream waters were collected from several sites near Peña de Hierro; this is the main source of the natural acid mine drainage characteristic of Rio Tinto. Figure 1 shows a context image of the Peña de Hierro sampling site and images of the four samples analyzed. The samples were collected from the banks of the stream as indicated in the figure and sealed in plastic bags bags in order to minimize transformation of the minerals. The pH in our sampling site was ~3 at the time samples were collected. The samples were analyzed in the laboratory within two weeks of collection. Although transformation of the samples was possible during storage and transport, we tried to minimize this through careful samples handling. Sample measurements were performed on the same samples and preparation for XRD was performed directly prior to measurement. In-situ mineralogical analyses of samples from the Rio Tinto site were conducted in other studies (Sobron et al., 2011).

X-Ray diffraction analyses

Powder X-ray Diffraction was performed using inXitu's Terra instrument, a field-portable version of the CheMin instrument chosen for flight on MSL (Blake et al., 2012; Sarrazin et al., 2008). Terra utilizes a CoKα X-ray tube, and its 2θ range is 4-55°. Samples were gently crushed and sieved prior to the analyses to achieve particles about 150 μm in size.

Mineral identification was carried out through peak comparison against the International Centre for Diffraction Data's (ICDD) Powder Diffraction File (PDF) mineral database. Quantitative results were obtained through Rietveld refinement or full pattern fitting techniques (Rietveld, 1969).

Visible-near infrared reflectance spectroscopy analyses

VNIR reflectance spectra were measured using a FieldSpec®ProFR from Analytical Spectral Devices (ASD) with a contact probe and solar simulated light source. Spectra were measured relative to a halon white reference from spots ~1 cm across on the rock surfaces at 2 nm spectral resolution from 0.35 to 2.50 µm. Spectra were collected at several locations on the rock surfaces without preparation. Minerals were identified by comparing the data with spectra of minerals in Bishop's library. Reflectance spectra of the natural samples are darker than the lab mineral spectra. This is because the natural samples are all rock surfaces, while the mineral spectra are all particulate samples.

Laser Raman spectroscopy analyses

The samples were placed on a 3D-motion stage of an inVia Raman microscope (Renishaw), and analyzed using 20× objective lenses. The 632.8 nm line from a Renishaw He-Ne laser was used as the excitation source. Laser power at the sample was measured as 1mW, and the spot size was 50 µm. The spectra were recorded within the region 100-3500 cm^{-1} with a spectral resolution of 4 cm^{-1}. Samples were analyzed without preparation. An average of five spots were analyzed on the surface of each of the samples; all of the spectra

recorded for each sample were averaged, thus yielding a single spectra per sample that accounts for inhomogeneities in the samples. The LRS spectra were analyzed in three regions of interest: low wavenumbers (100 to 800 cm^{-1}), mid wavenumbers (800 to 1300 cm^{-1}), and high wavenumbers (3100 to 3700 cm^{-1}). The spectra were filtered and baseline corrected using improved fast-Frourier transform algorithms. Routines based on the Marquardt method (Marquardt, 1963) were used to analyze the spectra in terms of band position, intensity, width and Gaussian-Lorentzian (G-L) factor (Sobron et al., 2008). The LRS spectra were interpreted in terms of the fundamental molecular vibrational modes that shape the spectral profiles.

RESULTS AND DISCUSSION

Figures 2 to 4 show the XRD pattern and the VNIR and LRS spectra of sample RTNP03, respectively. The XRD pattern of this sample is contributed mainly by gypsum, $CaSO_4 \cdot 2H_2O$. The additional peaks in this pattern are likely due to Na-jarosite, $NaFe^{3+}_3(SO_4)_2(OH)_6$ and quartz, SiO_2. The strong water combination bands in the RTNP03 VNIR spectra near 1.45 and 1.95 µm and the small shoulder near 1.76 µm are highly consistent with gypsum (Bishop et al., 2004). Jarosite contains features at 0.43, 0.89, 1.46, 1.85 and 2.26 µm (Bishop and Murad, 2005) that correspond well to the features observed in the spectra of RTNP03. Goethite exhibits a broader Fe^{3+} transition than jarosite and reflectance peaks at 0.59 and 0.76 µm (Bishop et al., 2004) that could be contributing to the RTNP03 spectra as well.

The Raman spectrum of sample RTNP03 corresponds to that of a sulfate rich minerals; it is mainly composed of bands arising from sulfate molecular vibrations and water. In aqueous systems, the v_1, v_2, v_3 and v_4 degenerate vibrational modes of sulfate give raise to bands at 982, 450, 1105, and 625 cm^{-1}, respectively (Nakamoto, 1997). A split of these sulfate vibrational modes into separate bands is observed in the crystal structures (Frost et al., 2005; Sasaki et al., 1998) and is due to symmetry breakdown. This effect is readily observed in the Raman spectra of samples RTNP03, particularly the splitting of the sulfate bands in the 1000-1300 cm^{-1} region. The two sets of bands centered around 450 and 600 cm^{-1} in the spectrum of RTNP03 are attributed to the v_2 and v_4 vibrational modes of the sulfate tetrahedral oxyanions, respectively. The above discussion applies to the Raman spectra of samples RTNP05, 07, and 10 discussed below.

The RTNP03 Raman spectrum shows characteristic features of jarosite in the high wavenumbers region: an intense band at 3401 cm^{-1} with two shoulders at 3367 and 3445 cm^{-1} (Chio et al., 2005; Frost et al., 2006). It is likely that additional bands are contributing to the complex the spectral envelope of sample RTPN03 in the high-wavenumbers region, incuding gypsum. The identification of the latter is, however, not unambigous. Finally, a strong band is observed at 386 cm^{-1}, attributed to a vibration of the $[Fe(H_2O)_6]^{2+}$ complex (Hester and Plane, 1964; Sobron et al., 2007). Based on our interpretation of the Raman spectrum, we suggest that sample RTNP03 is composed of jarosite, an unidentified hydrated Fe^{2+} sulfate, and possibly gypsum.

Figures 5 to 7 show the XRD pattern and the VNIR and LRS spectra of sample RTNP05, respectively. The XRD pattern of this sample is contributed mainly by gypsum, and shows peaks related to goethite, FeO(OH), and ferrihydrite, $Fe^{3+}_2O_3 \cdot 0.5(H_2O)$. Two areas of the RTNP05 samples were analyzed with VNRI reflectance. VNIR spectrum RTNP05_01 is consistent with jarosite, gypsum and goethite as in the spectra of sample RTNP03. VNIR spectrum RTNP05_02 lacks the jarosite features and exhibits broader water bands at shorter wavelengths and a broader Fe^{3+} band at longer wavelengths more consistent with ferrihydrite (Bishop and Murad, 2002) and ferricopiapite (Bishop et al., 2005). The Fe^{3+} reflectance peak near 0.6 μm is also consistent with goethite. However, these are not unique mineral assignments and other Fe-bearing minerals also have features that are similar.

Two Raman spectra, RTNP05a and RTNP05b were recorded from the RTNP05 sample; the LRS spectra are collocated with the VNIR spectra discussed above. The Raman spectrum RTNP05b shows two intense bands at 1006 and 1137 cm^{-1}. These bands are characteristic of gypsum (Krishnamurthy and Soots, 1971). The 412/491 cm^{-1} and the 617/668 cm^{-1} doublets originate from the degenerate sulfate v_2 and v_4 vibrational modes, respectively. Additionally, the pair of bands located in the water-stretching region around 3405 and 3491 cm^{-1} are indicative of the presence of two water molecules in the unit cell, consistent with gypsum.

The Raman spectrum RTN05a shows a sharp intense band at 3405 cm^{-1} with two shoulders at 3371 and 3443 cm^{-1}, consistent with jarosite (Chio et al., 2005; Frost et al., 2006). An

182 additional band is observed at 3497 cm^{-1}, likely related to additional water molecules
183 associated with other cations, *e.g.* gypsum. Based on the interpretation of the Raman
184 spectra recorded from sample RTNP05, our conclusion is that the RTNP05 sample contains
185 both jarosite and gypsum.

186 Figures 8 to 10 show the XRD pattern and the VNIR and LRS spectra of sample RTNP07,
187 respectively. The XRD pattern of sample RTNP07 includes contributions from copiapite,
188 jarosite, and quartz. The VNIR reflectance spectra of two spots on the surface of the
189 RTNP07 sample compare well to particulate samples of gypsum (JB556) <63 µm and
190 ferricopiapite (JB620) <125 µm. The Fe^{3+} bands at 0.43 and 0.87 µm are characteristic of
191 ferricopiapite (Bishop et al., 2005). The water bands at 1.44 and 1.93 µm are consistent
192 with a combination of ferricopiapite and gypsum, and the weak feature at 2.2 µm is
193 consistent with gypsum.

194 The complex envelope around 1000 cm^{-1} in the Raman spectrum of the RTNP07 sample
195 confirms the presence of multiple cation-sulfate bondings. The sharp band at 3526 cm^{-1}
196 may be assigned to Fe^{3+} or Fe^{2+}-OH vibrations, and the broad continuum around 3200 cm^{-1}
197 may be associated with water stretching vibrations; therefore, the RTNP07 sample
198 contains hydrous $Fe^{2+}$and Fe^{3+} oxides, likely belonging to the copiapite group, as suggested
199 by the XRD and VNIR reflectance analyses.

200 Figures 11 to 13 show the XRD pattern and the VNIR and LRS spectra of sample RTNP10.
201 The XRD pattern of this sample is contributed mainly by gypsum and quartz. Additional

peaks are likely due to Na-jarosite. The VNIR spectra of sample RTNP10 are highly consistent with gypsum, matching the triplet at 1.44, 1.49 and 1.54 μm, the bands near 1.75 and 1.94 μm, and exhibiting the doublet at 2.20 and 2.26 μm. Some ferrihydrite is likely present as well due to the broadening of the Fe^{3+} band near 0.9 μm and the water bands near 1.4 and 1.9 μm, and some goethite is consistent with these spectra due to the shoulder near 0.6 μm.

The Raman spectrum of the RTNP10 sample is similar to the spectrum RTNP05b in the low and mid wavenumbers regions. However, the RTNP10 Raman spectrum shows two sharp bands at 3405 and 3492 cm^{-1} at approximately the same position as those in the RTNP05b spectrum. The relative intensities of these pair of bands are, however, inverted in the RTNP10 spectrum. This is likely due to different crystal orientation – see (Iishi, 1979) for a detailed explanation of this phenomenon. Gypsum is the only mineral phase identified from the Raman spectrum of sample RTNP10.

PERFORMANCE ASSESSMENT OF THE THREE ANALYTICAL TECHNIQUES

Table 1 summarizes the results from the three techniques used for the analysis of the Rio Tinto sulfates. A range of mineral phases were detected within the samples, including jarosite, Na-jarosite, gypsum, goethite, copiapite, ferricopiapite, and ferrihydrite. The XRD technique detected quartz in some of the samples, however no traces of this component were detected by the other techniques. It is likely that the rock substrate underneath the sulfate layers contained quartz crystals. While VNIR reflectance and Raman, as non-destructive spectroscopic techniques, yielded information from the surface layers alone,

223 the powder used for the XRD analyses contained both sulfate layer and rock substrate
224 grains, and thus information from the latter is retrieved from the XRD patterns.

225 Raman detection of ferrihydrite and goethite is difficult when mixed with Fe^{2+} and Fe^{3+}
226 sulfates because sulfate and Fe-O interaction bands overlap in the low-wavenumber
227 region.

228 VNIR reflectance facilitated the identification of various sulfate compounds in each of the
229 samples, while XRD and Raman only provided positive identification of one or two
230 different phases; the VNIR reflectance spectra were measured from spots ~1 cm across,
231 notably increasing the probability of finding multiple components in a single spectrum.
232 On the other hand, such large spot size prevented the detection of microscopic inclusions
233 in the mineral matrices.

234 VNIR reflectance is uniquely suited for the characterization of water units and anions in
235 minerals; however, water is a very intense absorber and may mask the reflectance of the
236 cation-hydroxyl units (M-OH, where *M* represents a metallic cation). For this reason, the
237 identification of spectral features associated to hydrated minerals in the VNIR spectra is
238 not always unambiguous. One of the advantages of Raman is that water is a relatively
239 poor scatterer, and hence the hydroxyl stretching of the M-OH units can be better
240 resolved. As a result, more accurate band assignments can be achieved.

241 One of the difficulties associated with iron and sulfate-bearing compounds collected in
242 field-work is that they are often found to be poorly crystalline, making detection using

243 XRD and Raman spectroscopy difficult. In these instances, VNIR reflectance frequently
244 enables better detection of sulfate materials.

245 The small differences observed upon interpretation of the results from XRD, VNIR
246 reflectance, and Raman spectroscopy of four natural samples from the Rio Tinto Mars
247 analogue provide a complete picture of the mineralogical composition of the samples,
248 thus demonstrating that the three techniques are fully complementary and could be used
249 simultaneously for the characterization of sulfate and iron rich mineralogy without sample
250 preparation (except for XRD) and down to the crystal size (Raman).

251 In highly hydrated samples, Raman and XRD complement VNIR reflectance by
252 unambiguously identifying different phases. For poorly crystalline samples, VNIR
253 reflectance provides a more robust mineral identification, overcoming the difficulties
254 associated with XRD and Raman spectroscopy.

255 In summary: the combined use of the Raman, VNIR reflectance and XRD techniques is
256 widely justified for achieving unique mineral identification of Fe-bearing oxides and
257 sulfates on natural samples from acidic Mars analogue sites, and likely on samples from
258 Mars surface and surface. Synergyes between these three techniques should be explored
259 in the context of the science objectives of future Mars missions, *e.g.* ESA'a ExoMars and
260 NASA's Mars 2020 through assesing their potential to characterize other types of minerals
261 relevant to Mars exploration.

ACKNOWLEDGMENTS

This work was partially supported by the Research Council of Spain (CSIC) through grant no. UAC2005-007 and the NASA Astrobiology Institute through the Lewis and Clark Fund for Exploration and Field Research in Astrobiology. The authors thank Aurelio Sanz and Tayro Acosta for their valuable assistance in the collection and preservation of samples.

REFERENCES

Amils, R., Gonzalez-Toril, E., Fernandez-Remolar, D., Gomez, F., Aguilera, A., Rodriguez, N., Malki, M., Garcia-Moyano, A., Fairen, A.G., de la Fuente, V., and Sanz, J.L. (2007) Extreme environments as mars terrestrial analogs: The Rio Tinto case. Planetary and Space Science, 55(3), 370-381.

Amils, R., González-Toril, E., Fernández-Remolar, D., Gómez, F., Rodríguez, N., and Durán, C. (2002) Interaction of the sulfur and iron cycles in the Tinto River ecosystem. Reviews in Environmental Science and Biotechnology, 1(4), 299-309.

Bibring, J.-P., Arvidson, R.E., Gendrin, A., Gondet, B., Langevin, Y., Le Mouelic, S., Mangold, N., Morris, R.V., Mustard, J.F., Poulet, F., Quantin, C., and Sotin, C. (2007) Coupled Ferric Oxides and Sulfates on the Martian Surface. Science, 317(5842), 1206-1210.

Bishop, J.L., Dyar, M.D., Lane, M.D., and Banfield, J.F. (2005) Spectral identification of hydrated sulfates on Mars and comparison with acidic environments on Earth. International Journal of Astrobiology, 3(4), 275-285.

Bishop, J.L., and Murad, E. (2002) Spectroscopic and geochemical analyses of ferrihydrite from springs in Iceland and applications to Mars. Geological Society, London, Special Publications, 202(1), 357-370.

Bishop, J.L., and Murad, E. (2005) The visible and infrared spectral properties of jarosite and alunite. American Mineralogist, 90(7), 1100-1107.

Bishop, J.L., Murad, E., Lane, M.D., and Mancinelli, R.L. (2004) Multiple techniques for mineral identification on Mars: a study of hydrothermal rocks as potential analogues for astrobiology sites on Mars. Icarus, 169(2), 311-323.

Bishop, J.L., Parente, M., Weitz, C.M., Noe Dobrea, E.Z., Roach, L.A., Murchie, S.L., McGuire, P.C., McKeown, N.K., Rossi, C.M., Brown, A.J., Calvin, W.M., Milliken, R.E., and Mustard, J.F. (2009) Mineralogy of Juventae Chasma: Sulfates in the Light-toned Mounds, Mafic Minerals in the Bedrock, and Hydrated Silica and Hydroxylated Ferric Sulfate on the Plateau. Journal of Geophysical Research, 114(E00D09), doi:10.1029/2009JE003352.

Blake, D., Vaniman, D., Achilles, C., Anderson, R., Bish, D., Bristow, T., Chen, C., Chipera, S., Crisp, J., Des Marais, D., Downs, R., Farmer, J., Feldman, S., Fonda, M., Gailhanou, M., Ma, H., Ming, D., Morris, R., Sarrazin, P., Stolper, E., Treiman, A., and Yen, A. (2012) Characterization and Calibration of the CheMin Mineralogical Instrument on Mars Science Laboratory. Space Science Reviews, 170(1-4), 341-399.

300 Boston, P.J., Spilde, M.N., Northup, D.E., Melim, L.A., Soroka, D.S., Kleina, L.G., Lavoie,
301 K.H., Hose, L.D., Mallory, L.M., Dahm, C.N., Crossey, L.J., and Schelble, R.T. (2001) Cave
302 Biosignature Suites: Microbes, Minerals, and Mars. Astrobiology 1, 25-55.

303 Chio, C.H., Sharma, S.K., and Muenow, D.W. (2005) Micro-Raman studies of hydrous
304 ferrous sulfates and jarosites. Spectrochimica Acta Part A-Molecular and Biomolecular
305 Spectroscopy, 61(10), 2428-2433.

306 Christensen, P.R., Bandfield, J.L., Clark, R.N., Edgett, K.S., Hamilton, V.E., Hoefen, T.,
307 Kieffer, H.H., Kuzmin, R.O., Lane, M.D., Malin, M.C., Morris, R.V., Pearl, J.C., Pearson, R.,
308 Roush, T.L., Ruff, S.W., and Smith, M.D. (2000) Detection of crystalline hematite
309 mineralization on Mars by the Thermal Emission Spectrometer: Evidence for near-surface
310 water. J. Geophys. Res., 105(E4), 9623-9642.

311 Christensen, P.R., Morris, R.V., Lane, M.D., Bandfield, J.L., and Malin, M.C. (2001) Global
312 mapping of Martian hematite mineral deposits: Remnants of water-driven processes on
313 early Mars. J. Geophys. Res., 106(E10), 23873-23885.

314 Clegg, S.M., Mangold, N., Le Mouélic, S., Olilla, A., Anderson, R., Blaney, D.L., Clark, B.,
315 Cousin, A., Dyar, M.D., Ehlmann, B.L., Fabre, C., Forni, O., Lasue, J., Meslin, P.-Y., Schroder,
316 S., Sirven, J.B., Vaniman, D.T., Maurice, S., Wiens, R.C., and Team, M.S. (2013) High
317 Calcium Phase Observations at Rocknest with ChemCam. LPI Contributions, 1719, 2087.

Farrand, W.H., Glotch, T.D., Rice, J.W., Jr., Hurowitz, J.A., and Swayze, G.A. (2009) Discovery of jarosite within the Mawrth Vallis region of Mars: Implications for the geologic history of the region. Icarus, 204, 478-488.

Fernandez-Remolar, D.C., Morris, R.V., Gruener, J.E., Amils, R., and Knoll, A.H. (2005) The Rio Tinto basin, Spain: Mineralogy, sedimentary geobiology, and implications for interpretation of outcrop rocks at Meridiani Planum, Mars. Earth and Planetary Science Letters, 240(1), 149-167.

Fernández-Remolar, D.C., Prieto-Ballesteros, O., Gómez-Ortíz, D., Fernández-Sampedro, M., Sarrazin, P., Gailhanou, M., and Amils, R. (2011) Río Tinto sedimentary mineral assemblages: A terrestrial perspective that suggests some formation pathways of phyllosilicates on Mars. Icarus, 211(1), 114-138.

Flahaut, J., Quantin, C., Allemand, P., Thomas, P., and Le Deit, L. (2010) Identification, distribution and possible origins of sulfates in Capri Chasma (Mars), inferred from CRISM data. Journal of Geophysical Research: Planets, 115(E11), doi: E11007, 10.1029/2009JE003566.

Frost, R.L., Wills, R.A., Kloprogge, J.T., and Martens, W. (2006) Thermal decomposition of ammonium jarosite (NH4)Fe-3(SO4)(2)(OH)(6). Journal of Thermal Analysis and Calorimetry, 84(2), 489-496.

Frost, R.L., Wills, R.A., Weier, M.L., and Martens, W. (2005) Comparison of the Raman spectra of natural and synthetic K- and Na-jarosites at 298 and 77 K. Journal of Raman Spectroscopy, 36(5), 435-444.

Gellert, R., Rieder, R., Bruckner, J., Clark, B.C., Dreibus, G., Klingelhofer, G., Lugmair, G., Ming, D.W., Wanke, H., Yen, A., Zipfel, J., and Squyres, S.W. (2006) Alpha particle X-ray spectrometer (APXS): Results from Gusev crater and calibration report. Journal of Geophysical Research-Planets, 111(E2), E02S05.

Gendrin, A., Mangold, N., Bibring, J.P., Langevin, Y., Gondet, B., Poulet, F., Bonello, G., Quantin, C., Mustard, J., Arvidson, R., and LeMouelic, S. (2005) Sulfates in martian layered terrains: the OMEGA/Mars Express view. Science, 307(5715), 1587-1591.

Haskin, L.A., Wang, A., Jolliff, B.L., McSween, H.Y., Clark, B.C., Des Marais, D.J., McLennan, S.M., Tosca, N.J., Hurowitz, J.A., Farmer, J.D., Yen, A., Squyres, S.W., Arvidson, R.E., Klingelhofer, G., Schroder, C., de Souza, P.A., Ming, D.W., Gellert, R., Zipfel, J., Bruckner, J., Bell, J.F., Herkenhoff, K., Christensen, P.R., Ruff, S., Blaney, D., Gorevan, S., Cabrol, N.A., Crumpler, L., Grant, J., and Soderblom, L. (2005) Water alteration of rocks and soils on Mars at the Spirit rover site in Gusev crater. Nature, 436(7047), 66-69.

Hester, R.E., and Plane, R.A. (1964) Solvation of metal Ions in aqueous solutions: the metal-oxygen bond. Inorganic Chemistry, 3(5), 768-769.

Iishi, K. (1979) Phononspectroscopy and lattice dynamical calculations of anhydrite and gypsum. Physics and Chemistry of Minerals, 4(4), 341-359.

356 Johnson, J.R., Bell, J.F., Cloutis, E., Staid, M., Farrand, W.H., Mccoy, T., Rice, M., Wang, A.,
357 and Yen, A. (2007) Mineralogic constraints on sulfur-rich soils from Pancam spectra at
358 Gusev crater, Mars. Geophysical Research Letters, 34(13), L13202.

359 Klingelhofer, G., Morris, R.V., Bernhardt, B., Schroder, C., Rodionov, D.S., de Souza, P.A.,
360 Yen, A., Gellert, R., Evlanov, E.N., Zubkov, B., Foh, J., Bonnes, U., Kankeleit, E., Gutlich, P.,
361 Ming, D.W., Renz, F., Wdowiak, T., Squyres, S.W., and Arvidson, R.E. (2004) Jarosite and
362 hematite at Meridiani Planum from Opportunity's Mossbauer spectrometer. Science,
363 306(5702), 1740-1745.

364 Krishnamurthy, N., and Soots, V. (1971) Raman Spectrum of Gypsum. Canadian Journal of
365 Physics, 49(7), 885-896.

366 Lane, M.D., Bishop, J.L., Dyar, M.D., King, P.L., Parente, M., and Hyde, B.C. (2008)
367 Mineralogy of the Paso Robles soils on Mars. American Mineralogist, 93(5-6), 728-739.

368 Lichtenberg, K.A., Arvidson, R.E., Morris, R.V., Murchie, S.L., Bishop, J.L., Remolar, D.F.,
369 Glotch, T.D., Dobrea, E.N., Mustard, J.F., Andrews-Hanna, J., and Roach, L.H. (2010)
370 Stratigraphy of hydrated sulfates in the sedimentary deposits of Aram Chaos, Mars.
371 Journal of Geophysical Research-Planets, 115, E00D17.

372 Marquardt, D.W. (1963) An Algorithm for Least-Squares Estimation of Non-Linear
373 Parameters. Jornal of the Society for Industrial and Applied Mathematics, 11(2), 431-441.

374 Meslin, P.-Y., Gasnault, O., Forni, O., Schröder, S., Cousin, A., Berger, G., Clegg, S.M., Lasue,
375 J., Maurice, S., Sautter, V., Le Mouélic, S., Wiens, R.C., Fabre, C., Goetz, W., Bish, D.,

376 Mangold, N., Ehlmann, B., Lanza, N., Harri, A.-M., Anderson, R., Rampe, E., McConnochie,
377 T.H., Pinet, P., Blaney, D., Léveillé, R., Archer, D., Barraclough, B., Bender, S., Blake, D.,
378 Blank, J.G., Bridges, N., Clark, B.C., DeFlores, L., Delapp, D., Dromart, G., Dyar, M.D., Fisk,
379 M., Gondet, B., Grotzinger, J., Herkenhoff, K., Johnson, J., Lacour, J.-L., Langevin, Y., Leshin,
380 L., Lewin, E., Madsen, M.B., Melikechi, N., Mezzacappa, A., Mischna, M.A., Moores, J.E.,
381 Newsom, H., Ollila, A., Perez, R., Renno, N., Sirven, J.-B., Tokar, R., de la Torre, M., d'Uston,
382 L., Vaniman, D., Yingst, A., and Team, M.S. (2013) Soil Diversity and Hydration as Observed
383 by ChemCam at Gale Crater, Mars. Science, 341(6153).

384 Ming, D.W., Gellert, R., Morris, R.V., Arvidson, R.E., Brückner, J., Clark, B.C., Cohen, B.A.,
385 d'Uston, C., Economou, T., Fleischer, I., Klingelhöfer, G., McCoy, T.J., Mittlefehldt, D.W.,
386 Schmidt, M.E., Schröder, C., Squyres, S.W., Tréguier, E., Yen, A.S., and Zipfel, J. (2008)
387 Geochemical properties of rocks and soils in Gusev Crater, Mars: Results of the Alpha
388 Particle X-Ray Spectrometer from Cumberland Ridge to Home Plate. J. Geophys. Res.,
389 113(E12), E12S39.

390 Murchie, S.L., Mustard, J.F., Ehlmann, B.L., Milliken, R.E., Bishop, J.L., McKeown, N.K., Noe
391 Dobrea, E.Z., Seelos, F.P., Buczkowski, D.L., Wiseman, S.M., Arvidson, R.E., Wray, J.J.,
392 Swayze, G.A., Clark, R.N., Des Marais, D.J., McEwen, A.S., and Bibring, J.P. (2009) A
393 synthesis of Martian aqueous mineralogy after 1 Mars year of observations from the Mars
394 Reconnaissance Orbiter. J. Geophys. Res., 114, doi:10.1029/2009JE003342.

Nakamoto, K. (1997) Infrared and Raman Spectra of Inorganic and Coordination Compounds: Applications in coordination, organometallic, and bioinorganic chemistry. Wiley.

Parente, M., Bishop, J.L., and Bell, J.F. (2009) Spectral unmixing for mineral identification in Pancam images of soils in Gusev Crater, Mars. Icarus, 203(2), 421-436.

Rietveld, H. (1969) A profile refinement method for nuclear and magnetic structures. Journal of Applied Crystallography, 2(2), 65-71.

Roach, L.H., Mustard, J.F., Lane, M.D., Bishop, J.L., and Murchie, S.L. (2010) Diagenetic haematite and sulfate assemblages in Valles Marineris. Icarus, 207(2), 659-674.

Roach, L.H., Mustard, J.F., Murchie, S.L., Bibring, J.-P., Forget, F., Lewis, K.W., Aharonson, O., Vincendon, M., and Bishop, J.L. (2009) Testing Evidence of recent hydration state change in sulfates on Mars. J. Geophys. Res., 114(CRISM special issue), doi:10.1029/2008JE003245.

Sarrazin, P., Brunner, W., Blake, D., Gailhanou, M., Bish, D.L., Vaniman, D.T., Chipera, S.J., Ming, D.W., Steele, A., Midtkandal, I., Amundsen, H., and Peterson, R. (2008) Field Studies of Mars Analog Materials Using a Portable XRD/XRF Instrument. Lunar and Planetary Institute Science Conference Abstracts, 39, p. 2421.

Sasaki, K., Tanaike, O., and Konno, H. (1998) Distinction of jarosite-group compounds by Raman spectroscopy. Canadian Mineralogist, 36, 1225-1235.

414 Smith, P.H., Tamppari, L.K., Arvidson, R.E., Bass, D., Blaney, D., Boynton, W.V., Carswell, A.,
415 Catling, D.C., Clark, B.C., Duck, T., DeJong, E., Fisher, D., Goetz, W., Gunnlaugsson, H.P.,
416 Hecht, M.H., Hipkin, V., Hoffman, J., Hviid, S.F., Keller, H.U., Kounaves, S.P., Lange, C.F.,
417 Lemmon, M.T., Madsen, M.B., Markiewicz, W.J., Marschall, J., McKay, C.P., Mellon, M.T.,
418 Ming, D.W., Morris, R.V., Pike, W.T., Renno, N., Staufer, U., Stoker, C.R., Taylor, P.,
419 Whiteway, J.A., and Zent, A.P. (2009) H2O at the Phoenix Landing Site. Science, 325, 58-
420 61.

421 Sobron, P., Rull, F., Sobron, F., Sanz, A., Medina, J., and Nielsen, C.J. (2007) Modeling the
422 physico-chemistry of acid sulfate waters through Raman spectroscopy of the system
423 $FeSO_4$-H_2SO_4-H_2O. Journal of Raman Spectroscopy, 38(9), 1127-1132.

424 Sobron, P., Sansano, A., and Sanz, A. (2011) Evaporation pathways and solubility of Fe-Ca-
425 Mg-rich salts in acid sulfate waters. A model for Martian ancient surface waters. AGU Fall
426 Meeting Abstracts, 23, p. 1712.

427 Sobron, P., Sobron, F., Sanz, A., and Rull, F. (2008) Raman signal processing software for
428 automated identification of mineral phases and biosignatures on Mars. Applied
429 Spectroscopy, 62(4), 364-370.

430 Sowe, M., Wendt, L., McGuire, P.C., and Neukum, G. (2012) Hydrated minerals in the
431 deposits of Aureum Chaos. Icarus, 218(1), 406-419.

432 Tokar, R.L., Wiens, R.C., Maurice, S., Lasue, J., Johnson, J.R., Anderson, R.B., Cousin, A.,
433 Forni, O., Delapp, D.M., Lanza, N.L., Clegg, S.M., Bender, S.C., Barraclough, B.L., Dyar,

M.D., and Team, M.S. (2013) Searching for Chemical Variation Across the Surface of RockNest_3 Using MSL ChemCam Spectra. LPI Contributions, 1719, 1283.

Wang, A., Bell, J.F., Rice, M.S., and Cloutis, E.A. (2008) Coexistence of Si-rich and S-rich Materials at Gusev Crater, Columbia Hills. Lunar and Planetary Institute Science Conference Abstracts, p. 2186.

Wang, A., Haskin, L.A., Squyres, S.W., Jolliff, B.L., Crumpler, L., Gellert, R., Schröder, C., Herkenhoff, K., Hurowitz, J., Tosca, N.J., Farrand, W.H., Anderson, R., and Knudson, A.T. (2006) Sulfate deposition in subsurface regolith in Gusev crater, Mars. J. Geophys. Res., 111(E2), E02S17.

Weitz, C.M., Bishop, J.L., Thollot, P., Mangold, N., and Roach, L.H. (2011) Diverse mineralogies in two troughs of Noctis Labyrinthus, Mars. Geology, 39(11), 899-902, doi: 10.1130/G32045.1.

Wiseman, S.J., Arvidson, R.E., Morris, R.V., Poulet, F., Andrews-Hanna, J.C., Bishop, J.L., Murchie, S.L., Seelos, F.P., Des Marais, D., and Griffes, J.L. (2010) Spectral and stratigraphic context of hydrated sulfate and phyllosilicate deposits in Northern Sinus Meridiani, Mars. Journal of Geophysical Research, 115(CRISM special issue), E00D18, doi:10.1029/2009JE003354.

FIGURE CAPTIONS

Figure 1. Pictures of the sampling site, located at 37°43'18.69" N 6°33'33.24W, and pictures of the samples used for this study.

Figure 2. XRD pattern of sample RTNP03. The main peaks in the pattern match those of quartz (red), gypsum (blue), and Na-jarosite (green).

Figure 3. VNIR reflectance spectrum of sample RTNP03. The spectra compare to those of gypsum (JB556), jarosite (JB53), and likely goethite (JB54).

Figure 4. Raman spectrum (blue circles) of sample RTNP03 in three regions of interest, spectral bands (grey), and fitted spectrum (black). Jarosite, gypsum, and a hydrated iron sulfate were identified based on the position and relative intensity of the spectral bands.

Figure 5. XRD pattern of sample RTNP05. The main peaks in the pattern match those of gypsum (green), goethite (blue) and jarosite (red).

Figure 6. VNIR reflectance spectra of sample RTNP05. The spectra compare to those of gypsum (JB556), jarosite (JB53), goethite (JB54), ferrihydrite (JB499), and ferricopiapite (JB620). Unidentified Fe-bearing minerals may be present in the sample.

Figure 7. Raman spectra (blue circles) of sample RTNP05 in three regions of interest, spectral bands (grey), and fitted spectrum (black). Spectra 5a and 5b are offset for clarity. Jarosite and gypsum were identified based on the position and relative intensity of the spectral bands.

Figure 8. XRD pattern of sample RTNP07. The main peaks in the pattern match those of copiapite, jarosite, and quartz.

Figure 9. VNIR reflectance spectra of sample RTNP07. The spectra compare to those of gypsum (JB556) and ferricopiapite (JB620).

Figure 10. Raman spectrum (blue circles) of sample RTNP07 in three regions of interest, spectral bands (grey), and fitted spectrum (black). Hydrous iron oxides were identified based on the position and relative intensity of the spectral bands.

Figure 11. XRD pattern of sample RTNP010. The main peaks in the pattern match those of gypsum, quartz, and Na-jarosite.

Figure 12. VNIR reflectance spectrum of sample RTNP10 and database spectra of gypsum (JB556), goethite (JB54), and ferrihydrite (JB499).

Figure 13. Raman spectrum (blue circles) of sample RTNP10 in three regions of interest, spectral bands (grey), and fitted spectrum (black). Gypsum was identified based on the position and relative intensity of the spectral bands.

TABLE 1

Table 1. Summary of the mineral identification

	Sample ID			
	RTNP03	RTNP05	RTNP07	RTNP10
XRD	Gypsum	Gypsum	Copiapite	Gypsum
	Quartz	K-jarosite	K-jarosite	K-jarosite
	Na-jarosite		Quartz	Quartz

VNIR	K-jarosite Gypsum Goethite	K-jarosite Gypsum Goethite Ferrihydrite Ferricopiapite	Ferricopiapite Gypsum	Gypsum Ferrihydrite Goethite
LRS	K-jarosite UnID sulfate	Gypsum K-jarosite	Ferricopiapite	Gypsum

486


20 cm


RTNP03
RTNP05
RTNP07
RTNP10
2 cm

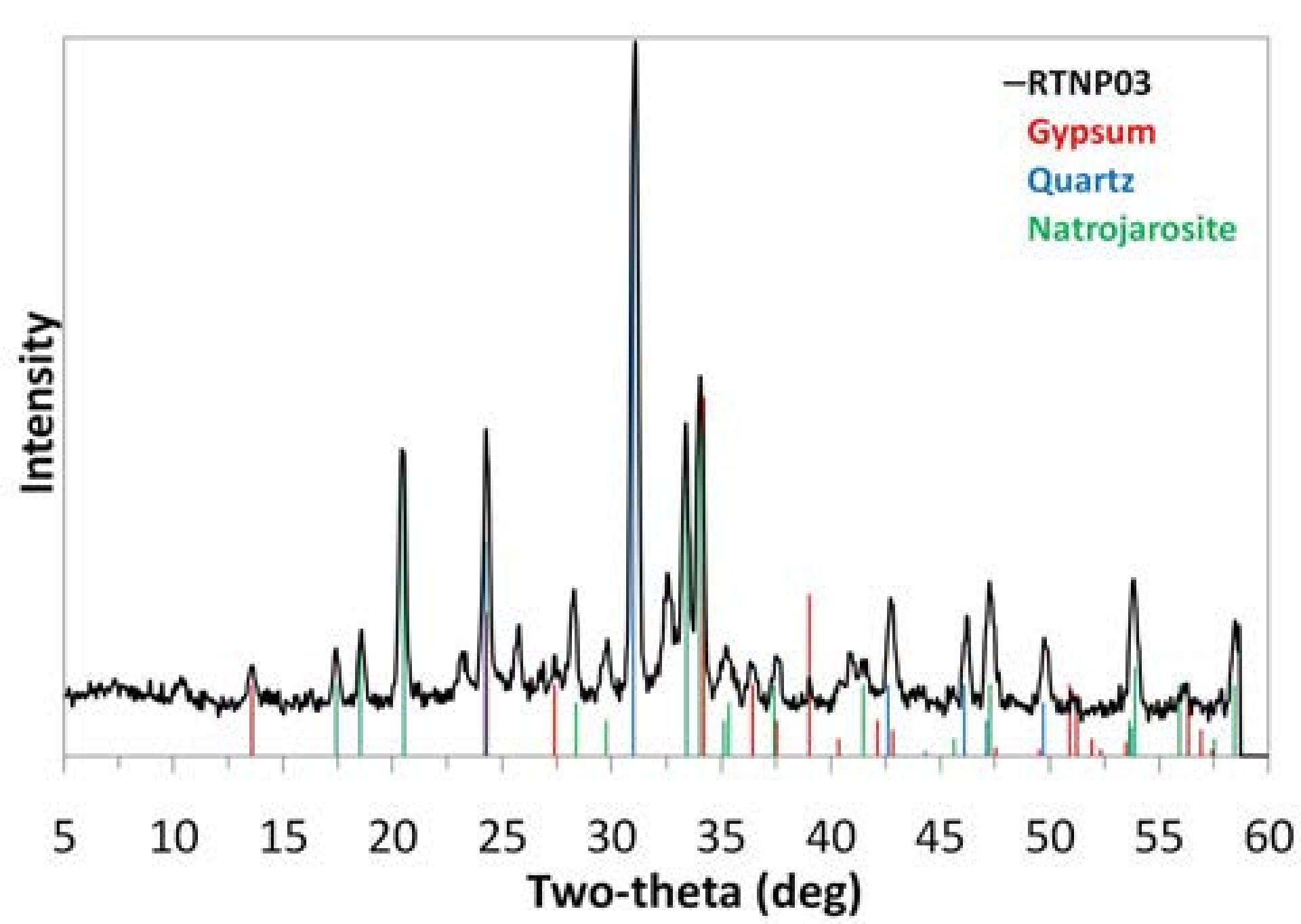
RTNP03
Gypsum
Quartz
Natrojarosite
Intensity
5
10
15
20
25
30
35
40
45
50
55
60
Two-theta (deg)

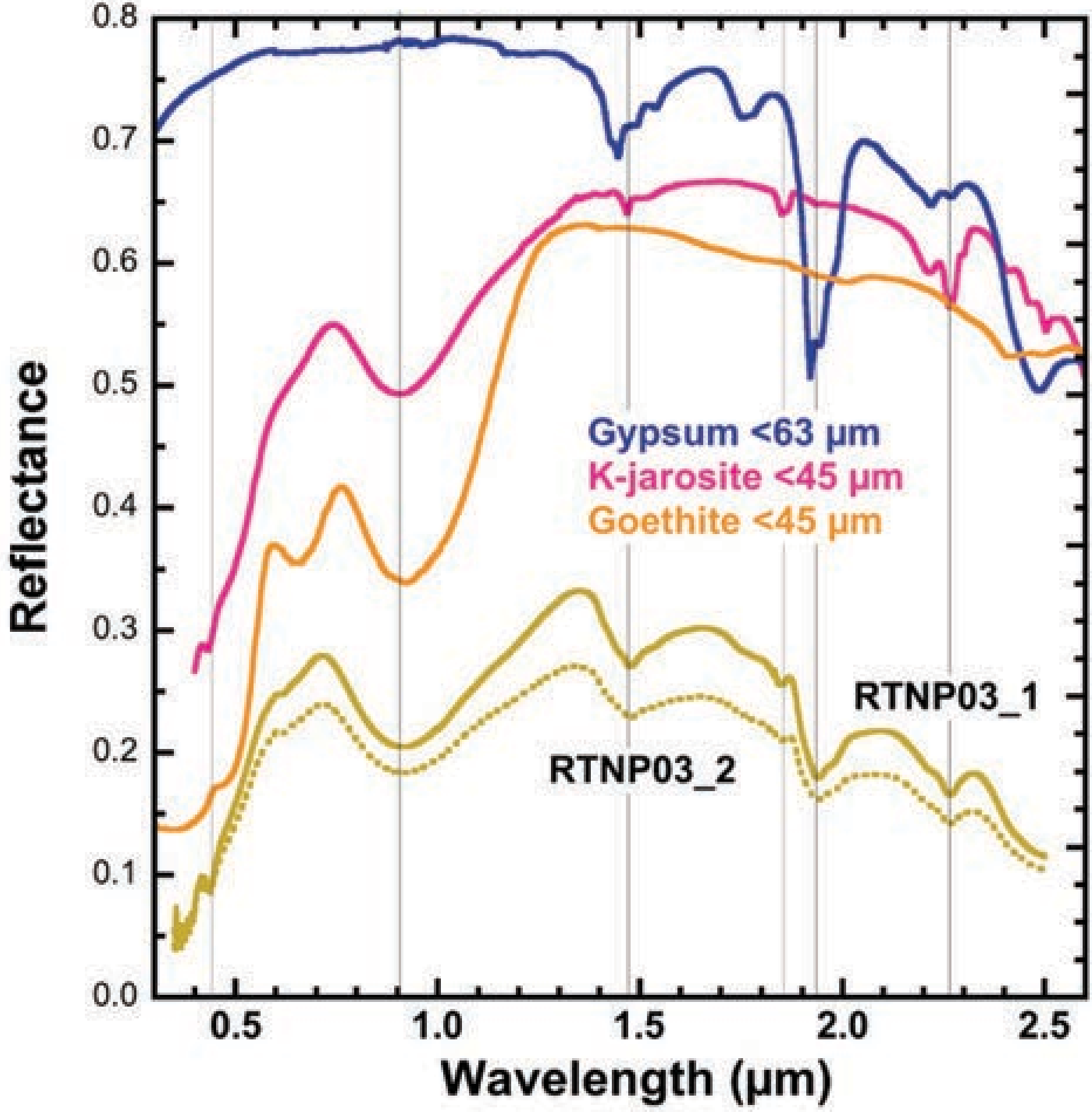
Reflectance
0.0
0.1
0.2
0.3
0.4
0.5
0.6
0.7
0.8
0.5
1.0
1.5
2.0
2.5
Wavelength (μm)
Gypsum <63 μm
K-jarosite <45 μm
Goethite <45 μm
RTNP03_1
RTNP03_2

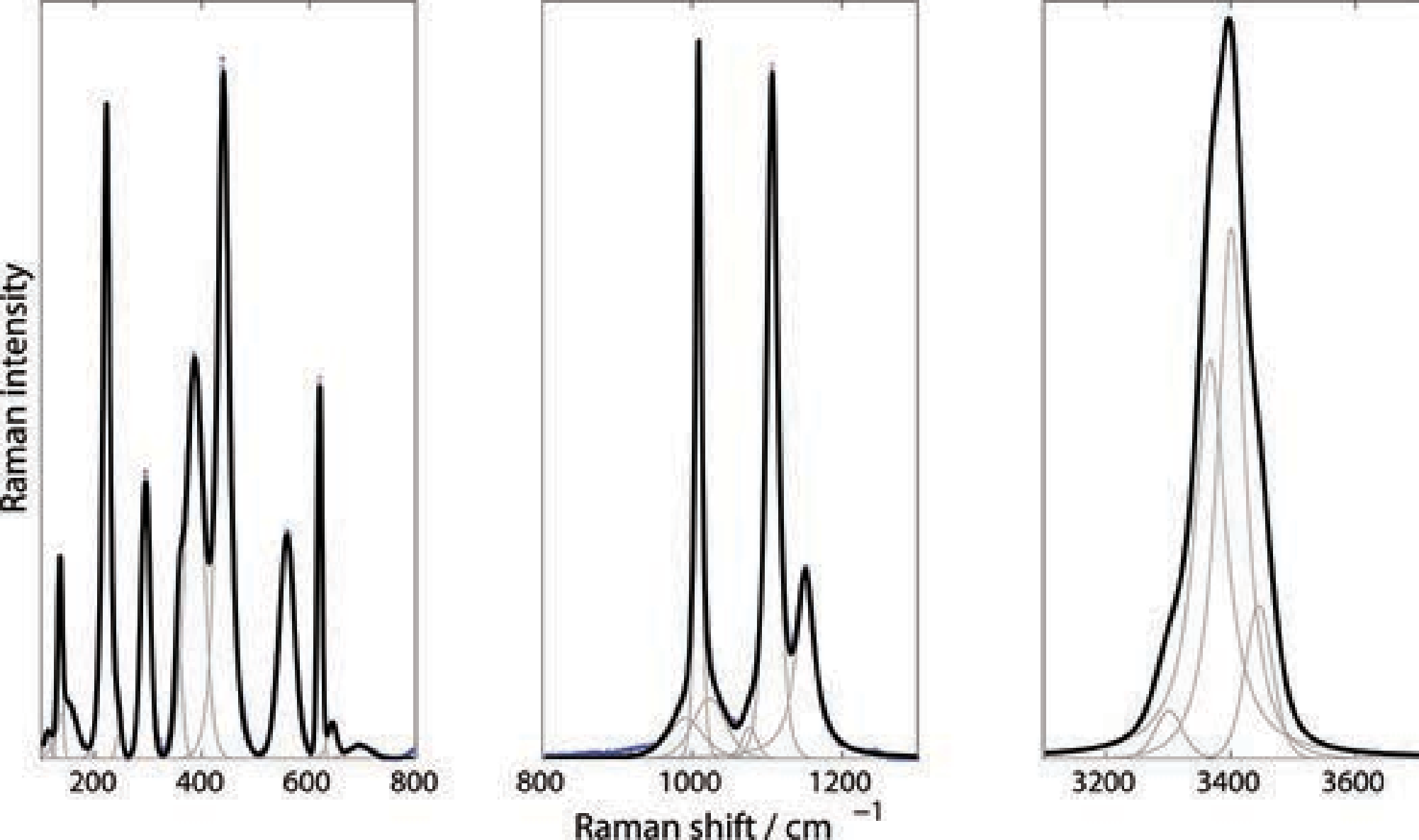
Raman intensity
200
400
600
800
800
1000
1200
3200
3400
3600
Raman shift / cm −1

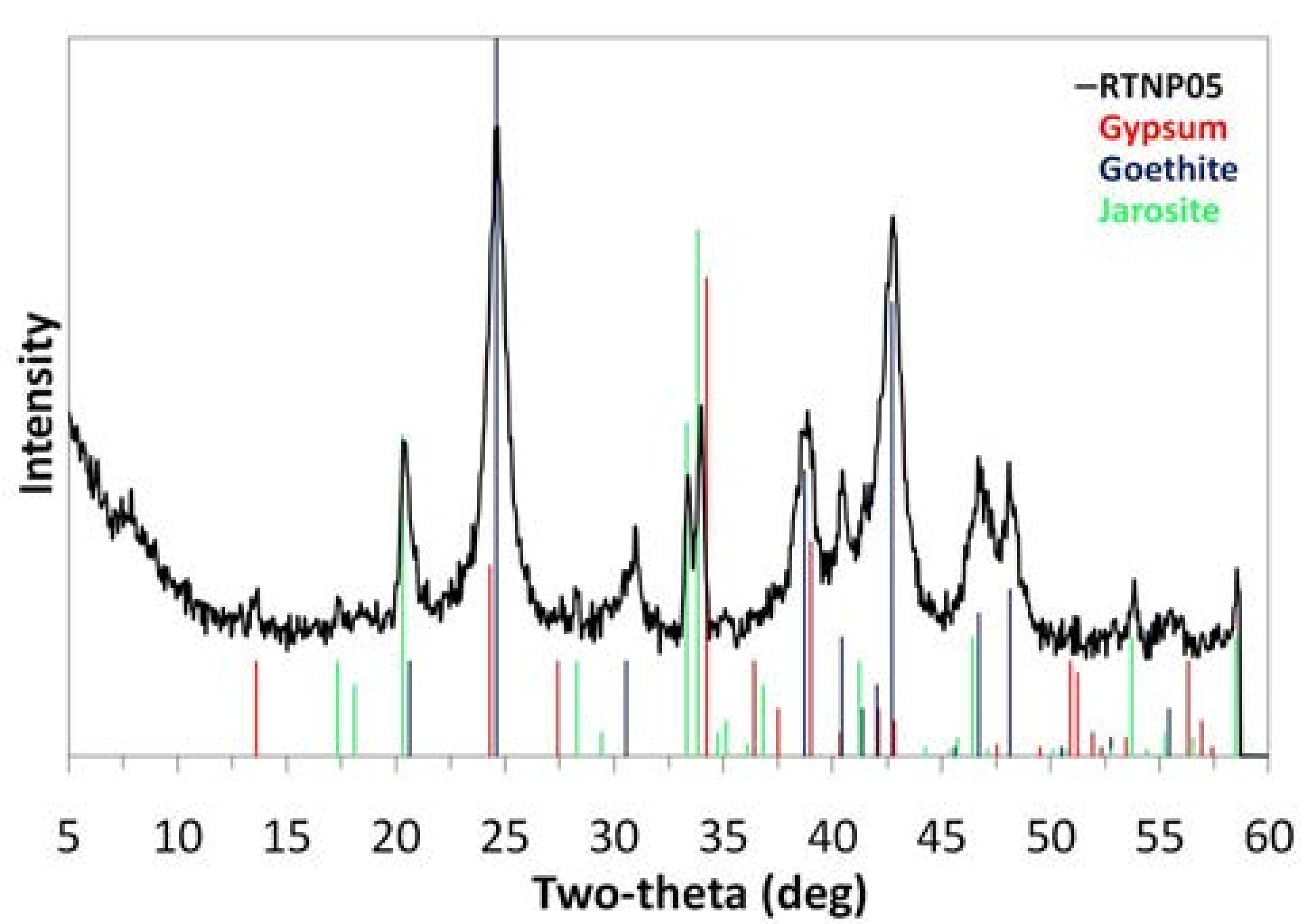
RTNP05
Gypsum
Goethite
Jarosite
Intensity
5
10
15
20
25
30
35
40
45
50
55
60
Two-theta (deg)

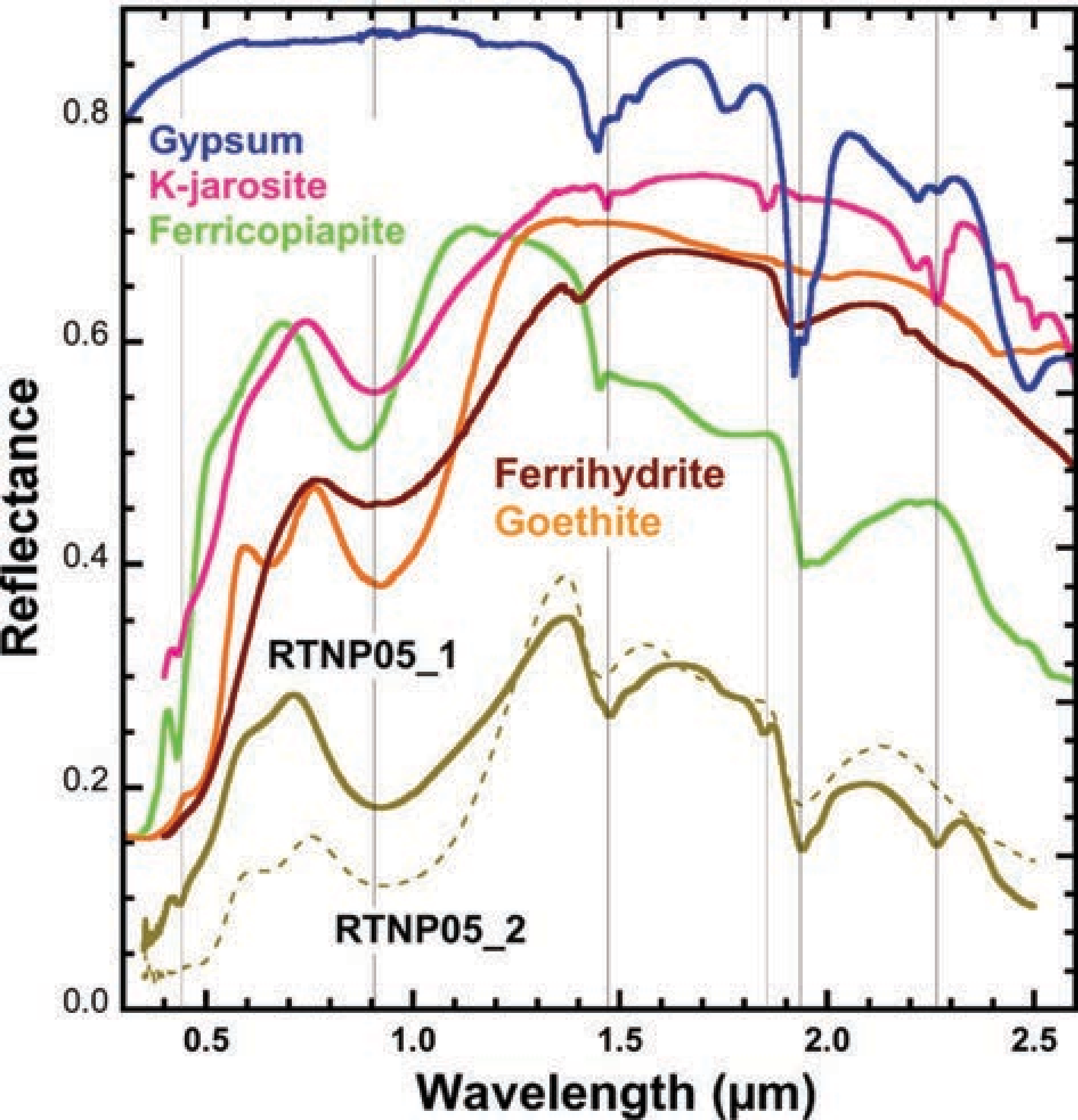
Gypsum
K-jarosite
Ferricopiapite
Ferrihydrite
Goethite
RTNP05_1
RTNP05_2
Reflectance
0.0
0.2
0.4
0.6
0.8
0.5
1.0
1.5
2.0
2.5
Wavelength (μm)

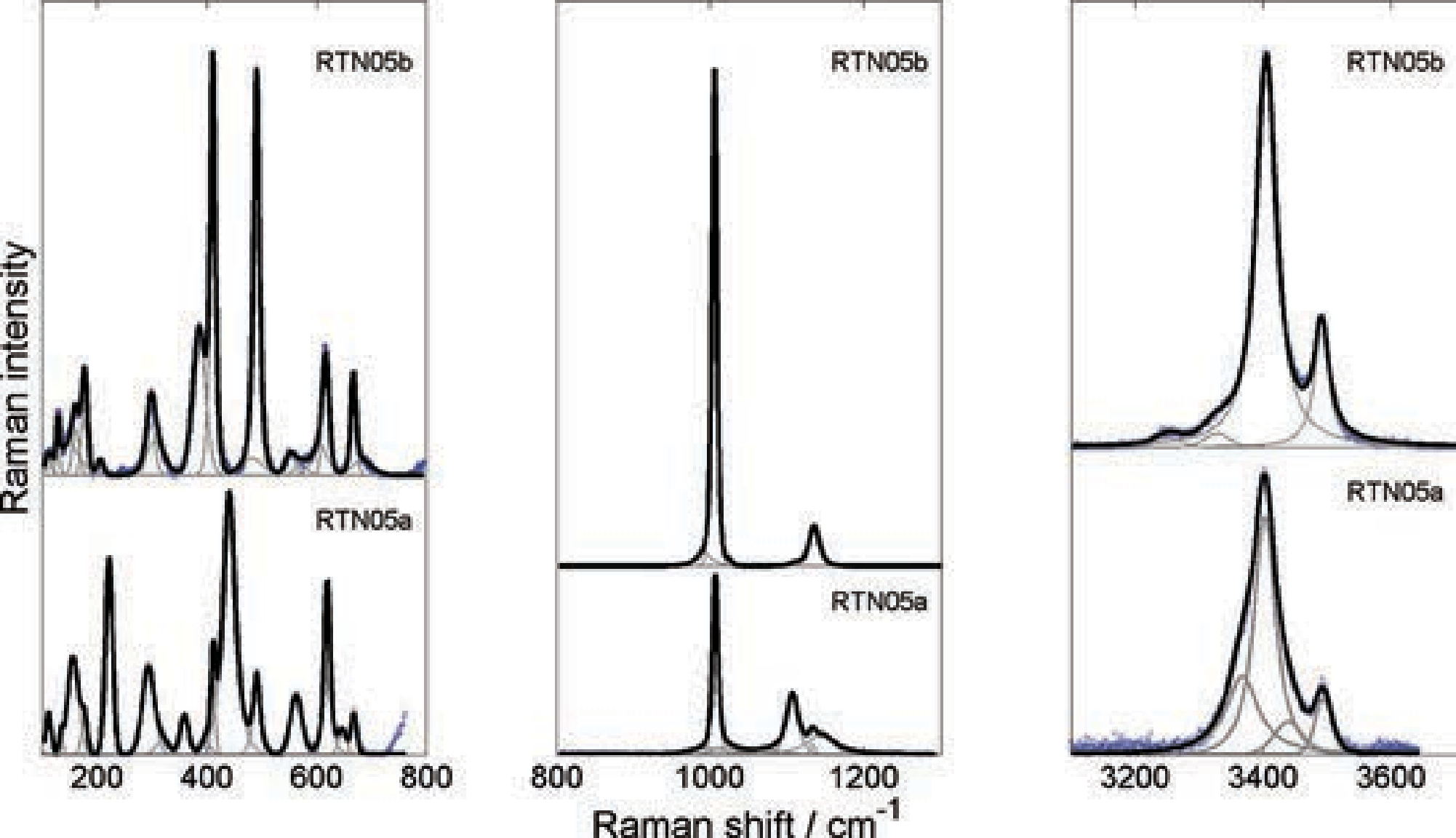
RTN05b
RTN05a
Raman intensity
200
400
600
800
RTN05b
RTN05a
800
1000
1200
RTN05b
RTN05a
3200
3400
3600
Raman shift / cm-1

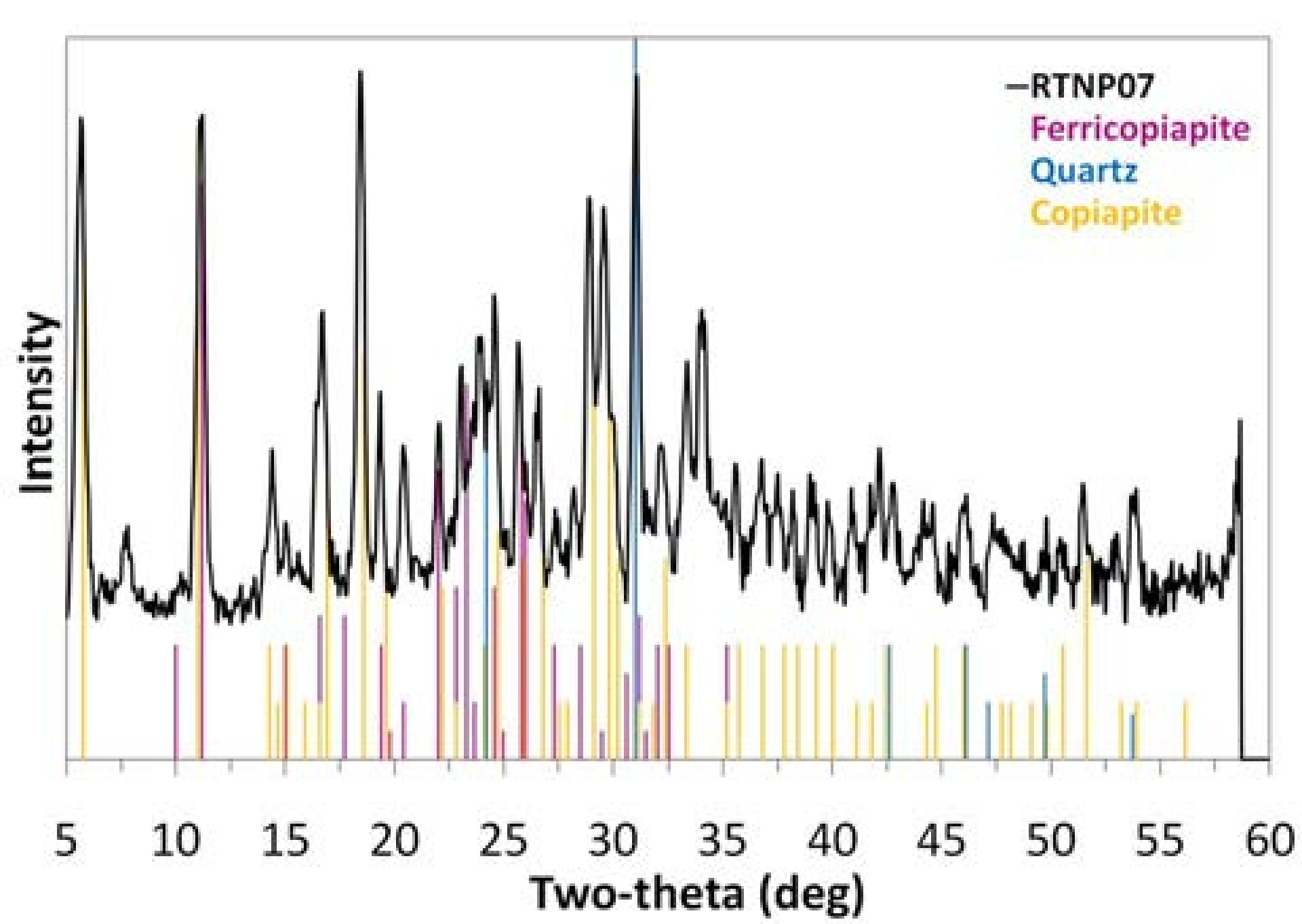
RTNP07
Ferricopiapite
Quartz
Copiapite
Intensity
5
10
15
20
25
30
35
40
45
50
55
60
Two-theta (deg)

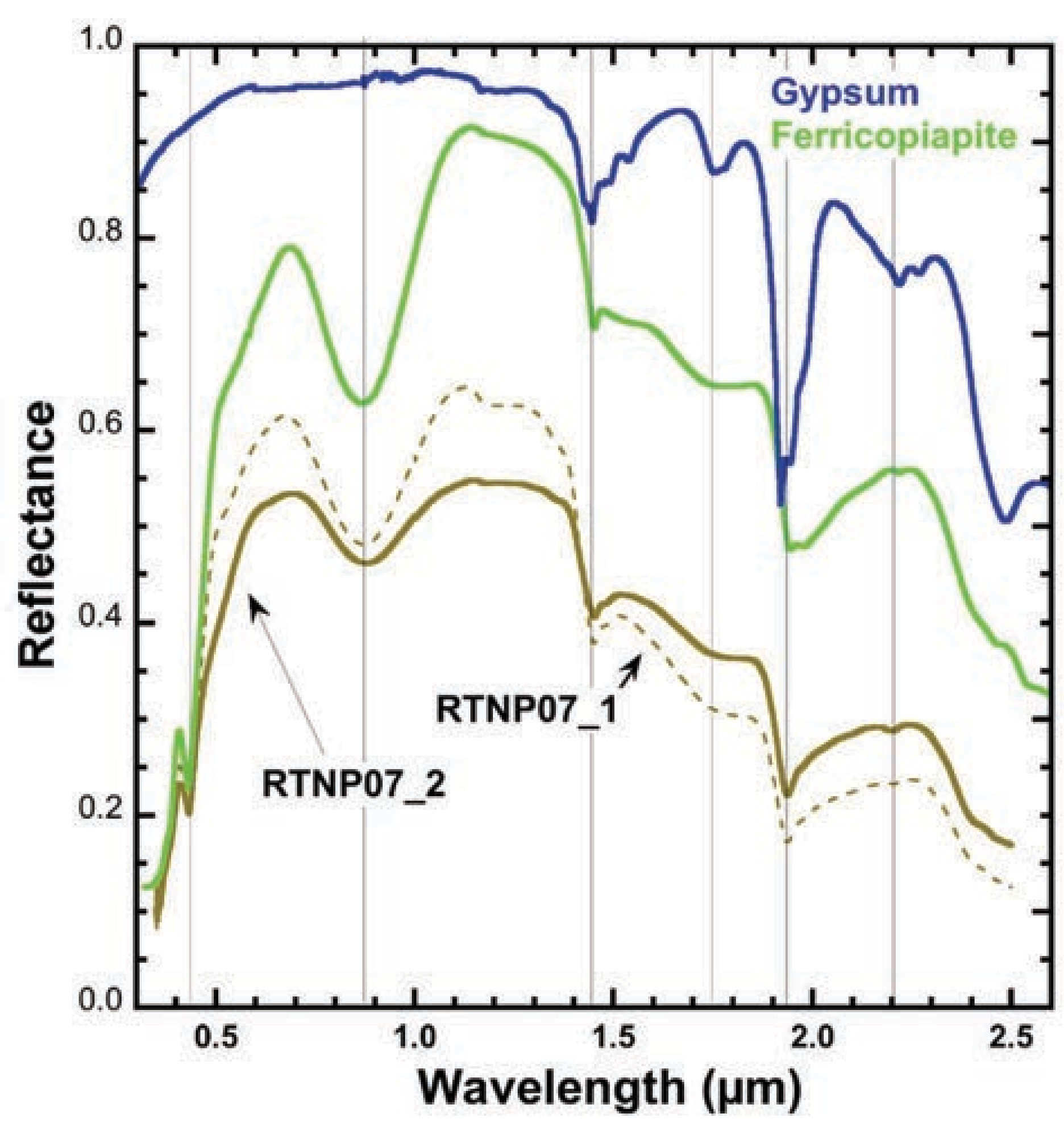
Gypsum
Ferricopiapite
RTNP07_1
RTNP07_2
Reflectance
Wavelength (μm)
1.0
0.8
0.6
0.4
0.2
0.0
0.5
1.0
1.5
2.0
2.5

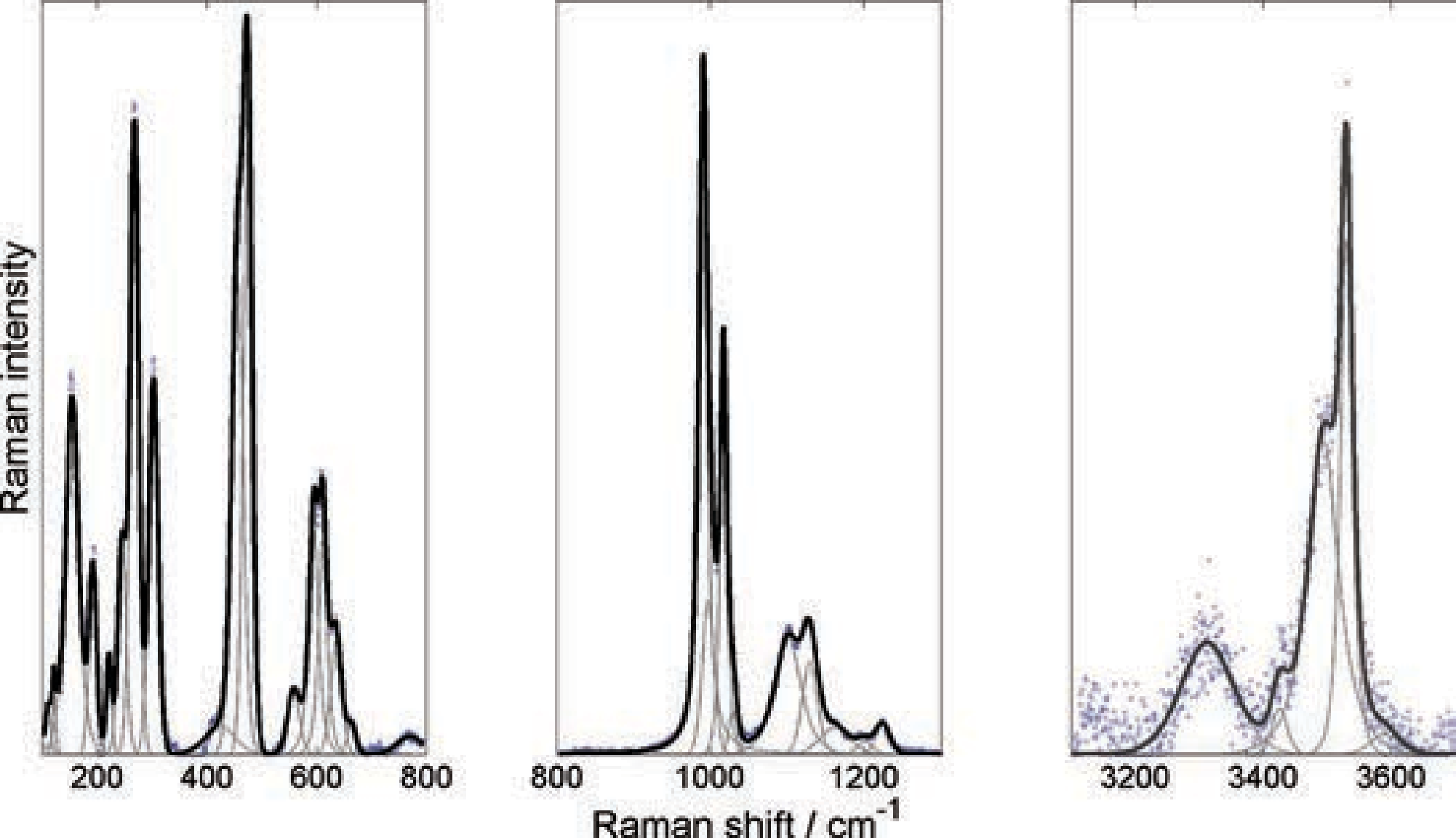
Raman intensity
200
400
600
800
800
1000
1200
3200
3400
3600
Raman shift / cm-1

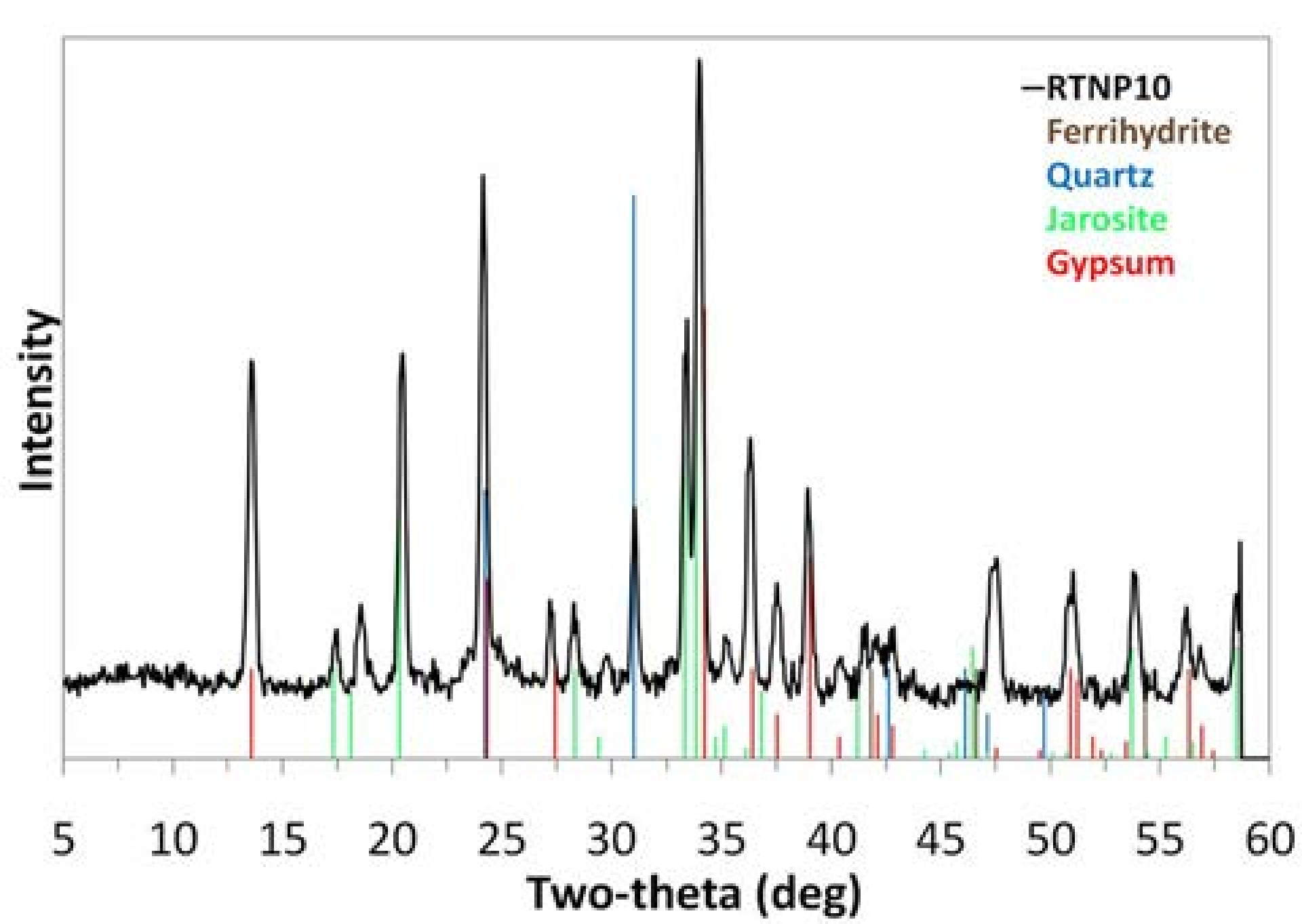
RTNP10
Ferrihydrite
Quartz
Jarosite
Gypsum
Intensity
5
10
15
20
25
30
35
40
45
50
55
60
Two-theta (deg)

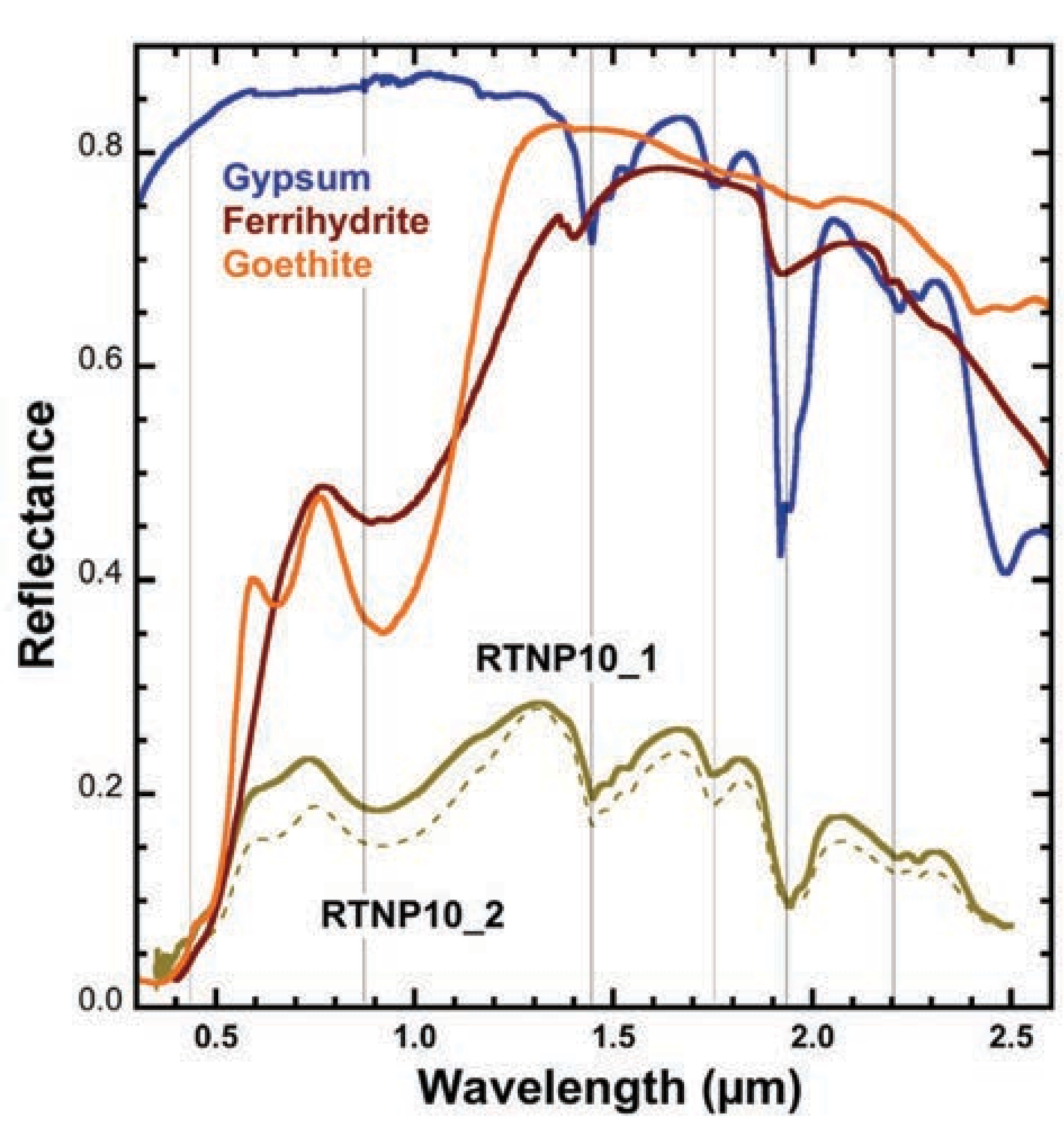
Gypsum
Ferrihydrite
Goethite
RTNP10_1
RTNP10_2
Reflectance
0.0
0.2
0.4
0.6
0.8
0.5
1.0
1.5
2.0
2.5
Wavelength (μm)

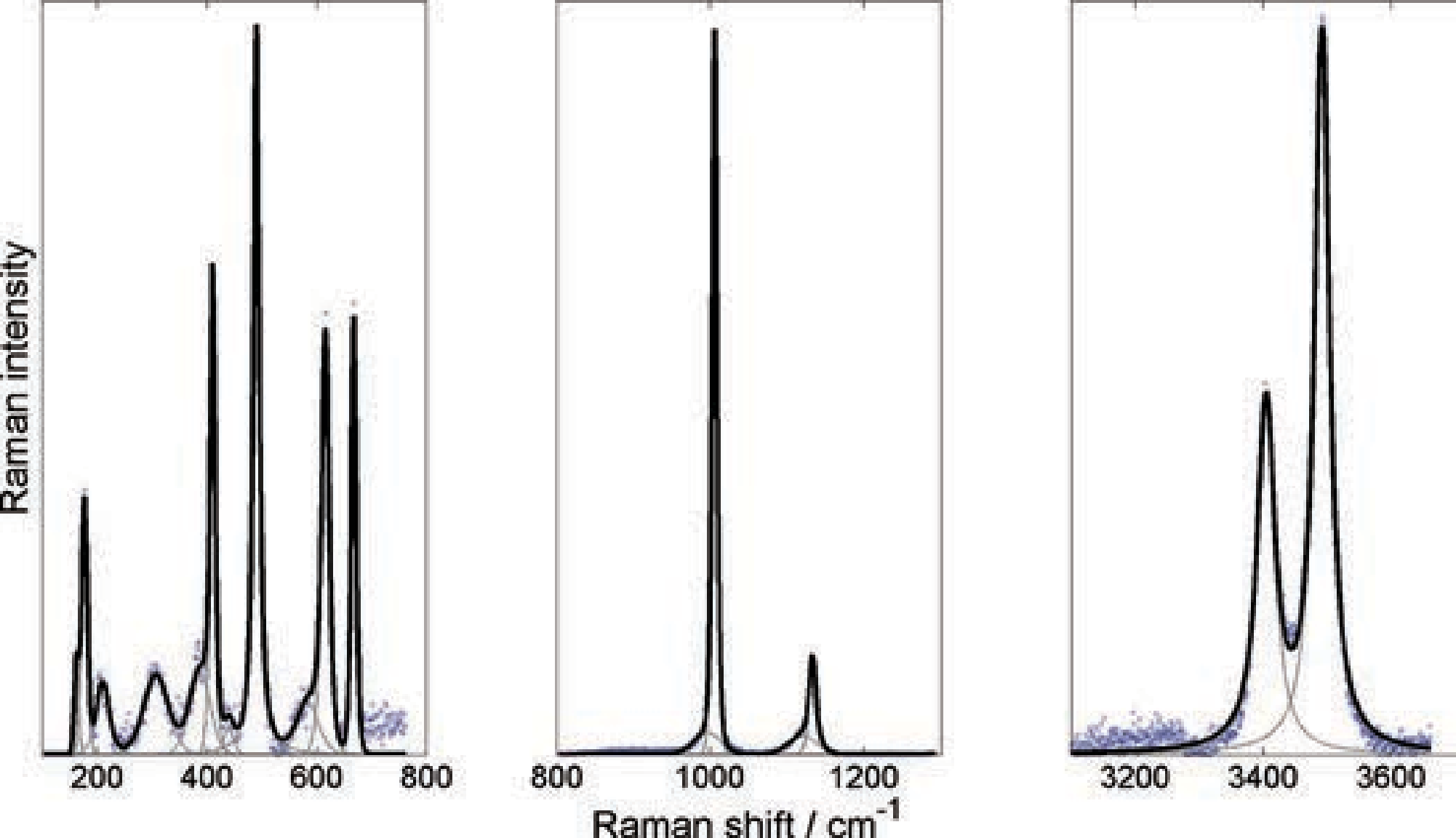
Raman intensity
200
400
600
800
800
1000
1200
3200
3400
3600
Raman shift / cm-1

Table 1. Summary of the mineral identification

	Sample ID			
	RTNP03	RTNP05	RTNP07	RTNP10
XRD	Gypsum	Gypsum	Copiapite	Gypsum
	Quartz	K-jarosite	K-jarosite	K-jarosite
	Na-jarosite		Quartz	Quartz
VNIR	K-jarosite	K-jarosite	Ferricopiapite	Gypsum
	Gypsum	Gypsum	Gypsum	Ferrihydrite
	Goethite	Goethite		Goethite
		Ferrihydrite		
		Ferricopiapite		
LRS	K-jarosite	Gypsum	Ferricopiapite	Gypsum
	UnID sulfate	K-jarosite		